This is an Accepted Manuscript of an article published by Taylor & Francis in Canadian Journal of Remote Sensing on 18/04/2016, available online: http://www.tandfonline.com/10.1080/07038992.2016.1177451.

Automated iceberg detection using high resolution X-band SAR images

Anja Frost, Rudolf Ressel, and Susanne Lehner

Deutsches Zentrum für Luft- und Raumfahrt (DLR), Maritime Safety and Security Lab of the Remote Sensing Technology Institute, Henrich-Focke-Straße 4, 28199 Bremen, Germany. Telephone 0049 421 24420-1851. Telefax 0049 421/5970-2421. {Anja.Frost@dlr.de; Rudolf.Ressel@dlr.de; Susanne.Lehner@dlr.de}

Abstract. Over northern latitudes, icebergs frequently cross shipping routes and impair marine traffic. To improve ship routing, we explore the capabilities of an algorithm that detects and charts icebergs from images provided by the German radar satellite TerraSAR-X. TerraSAR-X is in a near-polar orbit, equipped with an active X-Band radar antenna, and thus allows monitoring the ocean and frozen waters regardless of cloud cover and darkness. The algorithm we apply is based on the iterative censoring constant false alarm rate (IC-CFAR) detector, which has proven its usefulness for terrestrial target detection already. Different from the standard approach, we not only estimate statistical properties of open water intensities expressed by a probability density function, but also search for recurring patterns (i.e. waves). This allows discriminating icebergs from most false alarms that arise from rough sea and strong winds. Experiments carried out with a series of HH polarized TerraSAR-X Stripmap images acquired between 2012 and 2015 confirm that - due to consideration of wave pattern during image processing - the false alarm rate is reduced by a factor of three.

Résumé. Dans les régions de haute latitude, les icebergs croisent régulièrement les routes maritimes, gênant ainsi le trafic en mer. Afin d'améliorer le routage des navires, nous étudions un algorithme qui détecte et cartographie les icebergs à partir d'images radar du satellite allemand TerraSAR-X. TerraSAR-X est sur une orbite quasi-polaire. Il est équipé d'une antenne radar active en bande X, ce qui lui permet d'observer les océans et eaux glacées de jour comme de nuit et ce, quelle que soit la couverture nuageuse. L'algorithme que nous utilisons est basé sur le détecteur IC-CFAR qui a déjà prouvé son utilité pour la détection de cibles terrestres. Contrairement à l'approche habituelle, nous n'évaluons pas seulement les propriétés statistiques des intensités des eaux libres exprimées par une fonction de densité de probabilité, mais nous recherchons également des motifs récurrents (par exemple des vagues). Ceci permet de distinguer les icebergs de la plupart des fausses alertes dues aux mers agitées et aux forts vents. Les essais effectués sur une série d'images Stripmap à polarisation HH du satellite TerraSAR-X prises entre 2012 et 2015 confirment que le taux de fausses alertes est divisé par 3 grâce à la prise en compte des motifs des vagues pendant le traitement.

Introduction

Icebergs are pieces of freshwater ice that have broken away from marine glaciers and are floating in open water. The majority of the icebergs occurring in northern latitudes are calved from western Greenland glaciers, where they drift into Baffin Bay, circulating north along the Greenland and south along the eastern coast of Canada. Some also drift more southwards through the Davis Strait up to the Grand Banks (**Figure 1**). Estimated numbers of icebergs that have their source in Greenland range from 10,000 to 30,000 every year (Diemand, 2001). Although they are visually striking features in polar waters, they pose hazards to shipping and seabed structure (Buus-Hinkler et al., 2014).

To safeguard shipping, satellite-based synthetic aperture radar (SAR) is widely used. Equipped with an active radar antenna, SAR satellites provide image data of the ocean and frozen waters independent of weather conditions, cloud cover or daylight. In our work, we use image data provided by the radar satellite TerraSAR-X, which is in a near-polar orbit and fully operational since January 2008. Its X-band radar system provides image products with different spatial resolutions, scene sizes and polarizations as listed in **Table 1** (Eineder et al., 2008). **Figure 2** exemplifies a section of a TerraSAR-X image in HH polarization and shows icebergs in open water.

Figure 1. Main iceberg drift in northern latitudes (blue arrows) and acquisition areas selected for in the experiments (red rectangles)

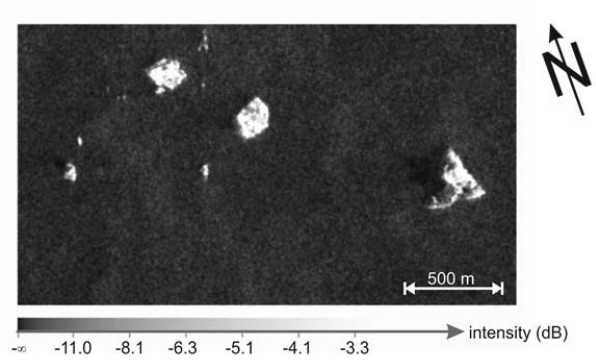

Figure 2. Section of a TerraSAR-X Stripmap image taken over Disko Bay, Greenland, 2013/04/23. Feature of the surface structure of icebergs are visible. Pinnacles appear bright on the right hand side, since the satellite was in right looking descending orbit (heading from North to South) during image acquisition.

In this paper, we explore the capabilities of a fully automatic algorithm to detect icebergs in TerraSAR-X Stripmap images. For detection, we make use of the constant false alarm rate (CFAR) detector, applying the iterative concept as mentioned by Ressel et al. (2015). Building on our previous work and on former studies in wind and sea state retrieval, we survey patterns in SAR images (i.e. waves) and integrate a new wave filter into our automated methodology. The wave filter improves the discrimination of icebergs from most false alarms that arise from rough seas and strong winds. In our experiments, we quantify the reliability of the algorithm, and the improvement brought about by the introduction of the wave filter.

In the following section, we briefly describe the standard CFAR detector and discuss its limitations when used for iceberg detection. Afterwards, we explain our iterative approach including the wave filter and present the test results.

Table 1. Specifications of selected TerraSAR-X imaging modes. Resolution and effective number of looks correspond to radiometrically enhanced images.

Mode		Stripmap, single polarized	Stripmap, dual polarized	ScanSAR, single polarized
Standard scene size		30 × 50 km²	15 × 50 km²	100 × 150 km²
Resolution				
in near range	(20°)	8.0 m	11.8 m	19.2 m
in far range	(45°)	7.0 m	9.9 m	17.0 m
Effective no. of looks				
in near range	(20°)	6.1	6.5	5.6
in far range	(45°)	6.4	6.6	11.1
Polarizations available		HH or VV	HH+HH or HH+HV or VV+VH	HH or VV or HV or VH

Standard CFAR detector

Numerous studies on iceberg detection from SAR images have been published to date. The CFAR detector is frequently applied and has proven its usefulness already for ship detection (Scharf, 1991; Vachon, 1997; Brusch, 2011) and later has been applied to iceberg detection (Power et al., 2001; Gill, 2001). Buus-Hinkler et al. (2014) utilized an adapted CFAR detector for studies on iceberg frequency in Greenland waters. Howell et al. (2004) applied the CFAR detector to multipolarized images and differentiated icebergs from ships. Gao et al. (2009) have introduced an iterative concept of the CFAR detector for terrestrial target detection in dense traffic situations; however, thus far it has not been applied to iceberg detection. In our previous work, we have adapted this iterative approach and applied to TerraSAR-X ScanSAR images containing a high iceberg density (Ressel et al., 2015).

Implementation details

The CFAR detector is designed to identify pixels whose intensity is unusually high when compared to the intensities in the surrounding image region (Scharf, 1991). That is, the detector performs pixel-based thresholding. The threshold calculation relies on a constant probability of false alarm (*PFA*) given by the user, as well as on assumptions about the expected probability density function of the intensity in the surrounding region (in our case: in open water). Generally, the threshold T is obtained by solving the relation

$$PFA = \int_T^\infty p(a)\,da \qquad (1)$$

where $p(a)$ represents the probability density function of the surroundings intensity.

The probability density function of the intensity of open water is usually assumed to be gamma- or k-distributed (Power et al., 2001; Gill, 2001; Buus-Hinkler et al., 2014; Bentes et al., 2014). In our work, we approximate with a Gaussian distribution, using the amplitude as random variable a. This approximation marginally impacts the performance of a CFAR-based detection from multi-looked SAR images (Truckenbrodt, 2012; Brusch et al., 2011). The

prime benefit of the Gaussian distribution is the fast computation of its parameters. This is crucial for any algorithm supporting operational, near real time services.

The parameters of the probability density function mean μ_{water} and standard deviation σ_{water} are estimated from a sliding window, which is fixed in size and hollow square shaped (**Figure 3**). Then, the threshold is set to *n*-times the standard deviation above the expected value of open water (Brekke, 2009):

$$T = \mu_{water} + n \cdot \sigma_{water} \quad (2)$$

Finally, a pixel is defined as part of an iceberg in case its amplitude is greater than the threshold *T*. Otherwise it is defined as open water.

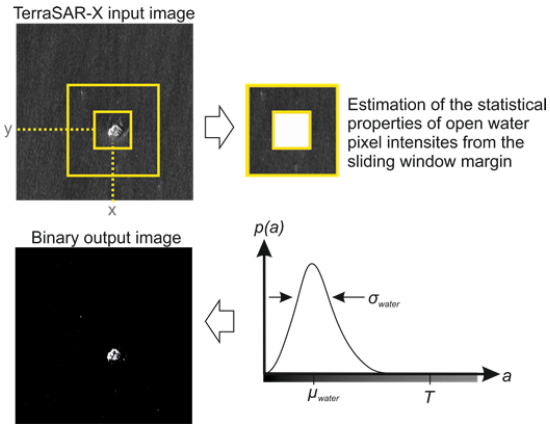

Figure 3. Principle of the CFAR detector. For each position (x,y), the statistical properties of open water are estimated, and the pixel at position (x,y) is set to iceberg (white) or open water (black).

Limitations

All thresholding methods fail once the backscatter intensities of icebergs overlap with those of open water. The intensity of open water depends on sea surface roughness; the higher the wind speed, the rougher the sea, the more the intensity of open water backscatter increases. **Figure 4** shows the expected mean intensities of open water for different wind speeds (5 m/s, 10 m/s, 15 m/s, and 18 m/s). They result from the geophysical model function XMOD, which was developed on the basis of an analysis of a large series of TerraSAR-X images with corresponding *in situ* measurements, e.g. buoys (Ren et al., 2012), and was adapted to HH polarized TerraSAR-X images by Shao et al. (2014). Additionally, **Figure 4** shows the mean intensity of 153 icebergs that have been identified manually from fourteen HH polarized TerraSAR-X images (as specified in **Table 2**). At wind speeds of 15 m/s, the intensities of open water pixels can equal the intensities of iceberg pixels. When image noise and variations caused by topographic differences in icebergs are taken into consideration, detection performance degrades.

The detection is even more affected in areas of high iceberg density. As soon as a neighboring iceberg is located in the sliding window, the estimated values μ_{water} and σ_{water} no longer

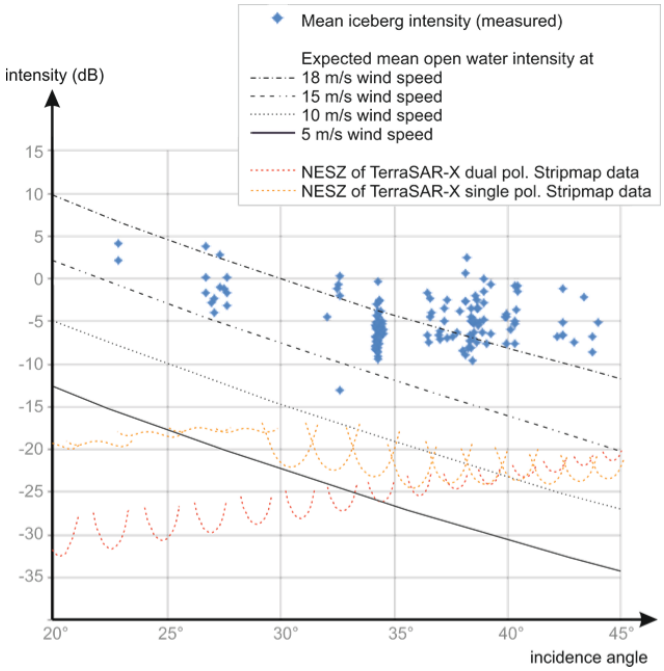

Figure 4. Mean intensity of 153 manually identified icebergs from 14 TerraSAR-X images in dependence of the local incidence angle (blue dots), expected mean intensity of open water for different upwind speeds (black lines), and noise floor (NESZ) of TerraSAR-X Stripmap images (red and orange line).

Table 2. Data sets. Each image was recorded in TerraSAR-X Stripmap mode and is radiometrically enhanced. In case of dual polarized image products, only the HH channel is processed. Single polarized image products are all taken in HH polarization. Details on the iceberg selection are given in the experimental results section.

Data set	Center coordinate	Date of acquisition	Center incidence angle	Polarisation
1	73.655, -58.876	2012/07/28	36.1°	Single pol.
2	73.725, -58.560	2012/07/29	26.2°	Dual pol.
3	73.698, -58.609	2012/08/03	32.7°	Dual pol.
4	73.682, -58.635	2012/08/24	42.9°	Single pol.
5	73.697, -58.615	2012/08/25	32.7°	Dual pol.
6	69.101, -51.881	2013/04/23	33.8°	Dual pol.
7	48.578, -52.988	2014/06/03	38.8°	Dual pol.
8	48.659, -51.592	2014/06/14	46.1°	Single pol.
9	48.334, -50.703	2014/06/17	24.0°	Single pol.
10	48.384, -52.770	2014/06/25	39.7°	Dual pol.
11	48.774, -52.872	2014/06/25	39.7°	Dual pol.
12	48.334, -50.705	2014/06/28	24.0°	Single pol.
13	48.675, -52.948	2015/06/04	39.3°	Single pol.
14	69.255, -51.208	2014/10/09	38.8°	Dual pol.

Data set	Location	Wind direction	Wind speed	Number of icebergs
1	Baffin Bay	135°	16.7 m/s	20
2	Baffin Bay	360°	5.8 m/s	12
3	Baffin Bay	338°	4.4 m/s	4
4	Baffin Bay	270°	1.4 m/s	10
5	Baffin Bay	338°	4.4 m/s	2
6	Disko Bay	67°	9.2 m/s	48
7	Grand Banks	90°	6.7 m/s	32
8	Grand Banks	28°	4.7 m/s	5
9	Grand Banks	35°	8.9 m/s	1
10	Grand Banks	21°	7.2 m/s	1
11	Grand Banks	21°	10.8 m/s	2
12	Grand Banks	4°	4.7 m/s	1
13	Bonavista Bay	90°	5.5 m/s	10
14	Disko Bay	135°	< 1 m/s	5

represent mean and standard deviation of open water pixel values, but of a mixture of open water and ice. In all likelihood, the values μ_{water} and σ_{water}, and therefore the threshold T, are too high. **Figure 5** illustrates how this can result in missed detections.

To sum up, in situations with high iceberg density, high wind speed or high sea state, thresholding techniques such as the standard CFAR detector reach their limits. The following section describes our approach.

Iterative iceberg detector

Iterative Concept

The more iceberg pixels are located in the sliding window, the more the threshold T increases. The example in **Figure 5** shows that within the iceberg cluster, many iceberg targets are missed, as the threshold T is too high. But as there are a few iceberg pixels that have been detected successfully, it is possible to steer the estimated values μ_{water} and σ_{water} towards the correct values, and detect formerly missed icebergs. Therefore, the CFAR detector is carried out iteratively.

In each iteration step, μ_{water} and σ_{water} are re-estimated. For re-estimation, we exclude pixels that have been identified in the previous iteration step to be part of an iceberg. In so doing, the new estimate is less corrupted and more iceberg pixels get detected.

In **Figure 6**, the iterative process is tested with the example iceberg cluster of **Figure 5**. After two iteration steps, all icebergs are detected. Obviously, the estimated values μ_{water} and σ_{water} converge towards the correct mean and standard deviation of open water pixel values. In future work, we want to investigate the convergence rate and develop stopping criteria. For the experiment in this paper, the number of iterations is fixed to two.

In order to minimize the computing time, we only re-estimate μ_{water} and σ_{water} in the regions surrounding detected iceberg pixels, since the other areas will not undergo a change.

Figure 7 illustrates the flow of our algorithm. After each iteration step, the output image is copied to a mask in order to save pixels that have to be excluded in the next re-estimation.

Front side driven region growing

The aim of region growing is to find all pixels that belong to one iceberg. Contiguous iceberg pixels are merged into one region. In this section, we describe a new front side driven region growing and also respond to the question of how to choose the design parameter n in equation (2).

The example in **Figure 8** shows that a low design parameter (n=5) in practice results in many false alarms. But apart from this fact, it makes it possible to map each iceberg as one solid region. n=15 keeps a low false alarm rate, but several iceberg pixels are missed. To combine the benefit of both, a low and a high design parameter n, we first execute the CFAR detector with n=15. Thereby, some pixels in each iceberg get detected,

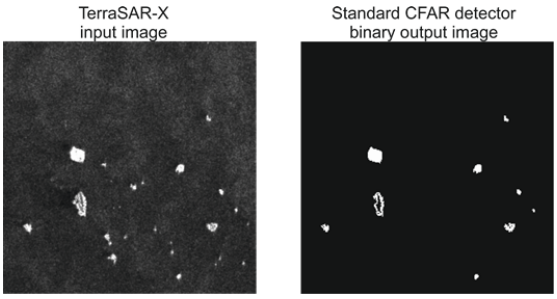

Figure 5. Standard CFAR detector applied to a section of a TerraSAR-X image with high iceberg density (Disko Bay, Greenland, 2013/04/23). Several icebergs remain undetected.

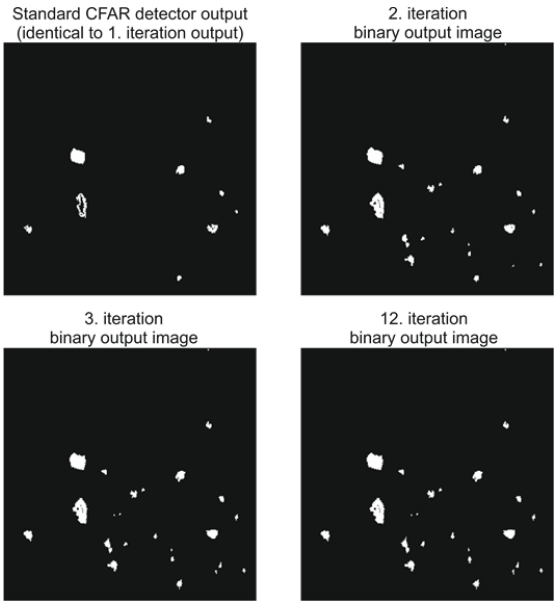

Figure 6. Iterative CFAR detector applied to the example image shown in **Figure 5**. Formerly missed icebergs get detected.

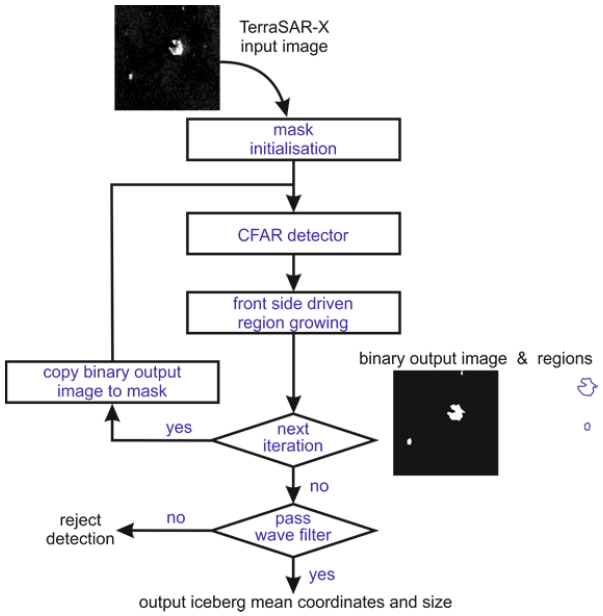

Figure 7. Flow chart of the iterative iceberg detector.

frequently those from the bright front side facing towards the radar. Then, starting with the detected front side pixels, region growing is carried out that includes all pixels with an intensity above a second threshold calculated with n=5. **Figure 8** (on the bottom right) illustrates how false alarms vanish and icebergs are mapped more accurately.

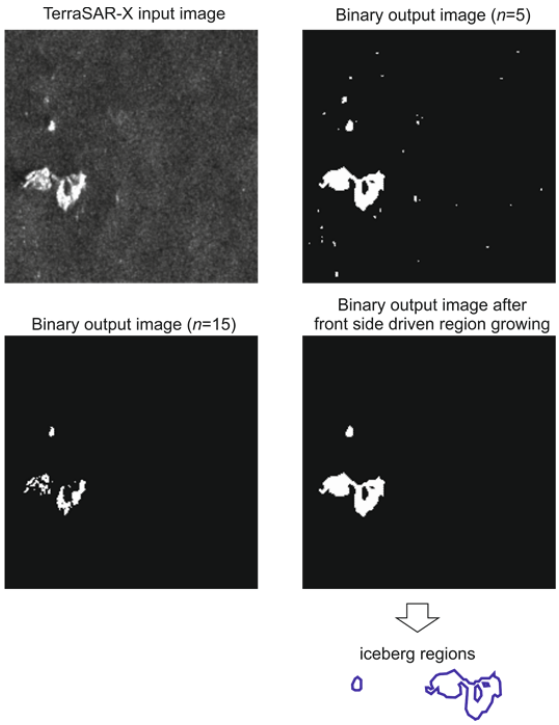

Figure 8. Optimization by front side driven region growing. Iceberg mapping is more accurate. The false alarm rate is kept down.

Wave filter

Even though the front side driven region growing ensures a low false alarm rate, it is not possible to avoid false alarms that arise from high wind speeds and rough seas. The intensity of wave crests can tend towards the intensity of icebergs (**Figure 9**, top row). Moreover, in some cases the ocean surface shows vertical smears of high intensity (**Figure 9**, bottom row). These smears and wave crests are frequently detected as icebergs.

We propose a CFAR-related filter, which additionally recognizes recurring patterns in the surroundings of detections. μ_{water} and σ_{water} are re-estimated from an area, which is no longer hollow squared shaped. It now gets the same outer shape of the detected object, but increased size (draft in **Figure 9**). By this means, in case of wave crests and smears, the estimation area is narrow and mainly captures pixels that belong to the same wave crest or smear. Accordingly, the detected object is no longer unusually bright. We can proceed from the assumption that most smears go undetected, that is, they are filtered out. In contrast, for most icebergs the estimation area is expanded in range and azimuth direction. The re-estimate differs minimally from the output of the hollow square shaped sliding window. Icebergs are detected again.

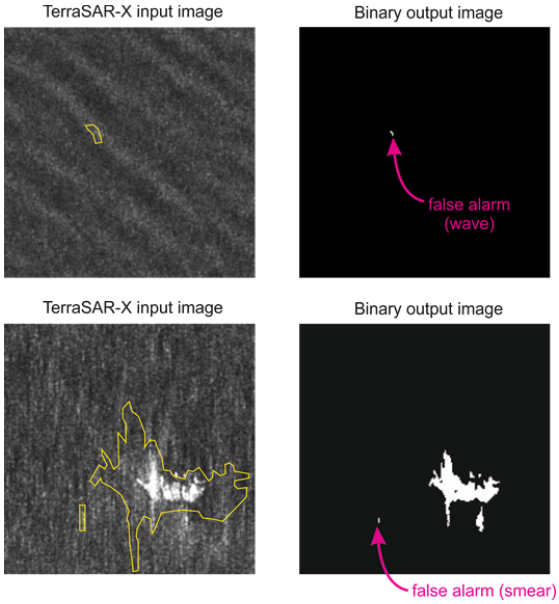

Figure 9. Basic idea of the wave filter. For each detected object, the CFAR detector is executed again. Different from **Figure 3**, the area used for estimating the statistical properties of the surroundings gets the same outer shape as the detection, but increased size (yellow lines). Its inner limit is given by the boundary of the detection itself. For most icebergs, the reshaping hardly makes a difference, i.e. they get detected again. But false alarms e.g. occurring at waves are no longer unusually bright compared to the pixels in the estimation area. They go undetected.

The idea of using a nonrectangular shaped sliding window has been mentioned by El-Darymli et al. (2013). Principe et al. (1995) used a gamma kernel instead of the hollow square shaped sliding window. In our work, we fit the shape individually to each detection.

Mask initialization

After each iteration step, the binary output image is copied to a mask in order to save pixels that have to be excluded in the next re-estimation step. Similar to Gao et al. (2009), the mask is initialized with a binary image generated from the input SAR image using a global threshold. This is done to speed up the iterative approach.

In our work, the global threshold is given by a priori knowledge about the gradient of icebergs and open water. The gradient is generally high at the edge of an iceberg, and also within an iceberg. In open water, low gradient values predominate. In former studies, e.g. Lehner et al. (2014); Ressel et al. (2015), gradient related features are used to classify different ice types. Here, the binarized gradient is used to initialize the mask.

Experimental Results

Quantitative analysis of the reliability

The figures presented above have visually highlighted the benefit of the iterative iceberg detector. In the following, we analyze the reliability of the detector quantitatively.

The experiment deals with 14 TerraSAR-X images listed in **Table 2**. We chose data sets that cover different weather and sea state conditions. Reported wind speeds and wind directions come from nearby weather stations.

The complete TerraSAR-X scenes are examined, except for data set 6, 7, 13, and 14. Data set 6 depicts more than 4000 icebergs. We selected an ROI the size of 4.8 km × 5.8 km. It contains 48 icebergs. For data set 7, the ROI spans 30 km × 15 km including 32 icebergs. For the data sets 13 and 14, *in situ* observations of icebergs are available in ROIs covering 30 km × 36 km (data set 13) and 0.5 km × 0.18 km (data set 14). Icebergs in the other data sets (1-12) have been identified manually by visual inspection of the TerraSAR-X image.

Two iteration steps are carried out, followed by the filter (that can be seen as a third iteration).

Table 3 summarizes the results. 153 icebergs have been identified manually from the images. Of these, 137 icebergs have been detected successfully, i.e. the detection rate of our algorithm amounts to 137/153 = 0.895. 16 icebergs were missed.

The lengths of the selected 153 icebergs range from 15 m (size category: small) to 650 m (size category: very large). In future work, we want to analyze the detection rate depending on different iceberg sizes.

Most false alarms arise from data set 1, which captures the highest wind speed (16.7 m/s). Here, 41 smears passed the wave filter. Nonetheless, it must be pointed out that without the filter, data set 1 would have yielded 117 false alarms. The other data sets (2-14) contain 24 false alarms before and 9 false alarms after filtering. Altogether, there remain 50 false alarms, which is equivalent to 0.003 false alarms per km².

In **Figure 10**, the overall detection rate and false alarm rate of our iterative iceberg detector are compared with the output of the standard CFAR detector carried out with a varying design parameter *n,* as well as with the iterative iceberg detector run without the wave filter. The high detection rate of the iterative iceberg detector (with wave filter) is achievable with the standard CFAR detector at n<10, but this is accompanied by a false alarm rate at least five times higher than the false alarm rate of the iterative detector. The standard CFAR detector shows a low false alarm rate at n=15, but the detection rate is significantly reduced. The wave filter reduces the false alarm rate of the iterative iceberg detector by approximately a factor of three, while the detection rate is decreased only marginally.

Computing time

All data sets were processed on a 2.2 GHz quad core CPU. On average, the computing time amounts to 12 minutes per Stripmap image, though it can extend in case many icebergs (>> 1000) are present; beginning with the second iteration, the computing time depends on the number of detections, because μ_{water} and σ_{water} are re-estimated in the surrounding region of detected iceberg pixels. The higher the number of detected pixels is, the more re-estimations have to be carried out.

Table 3. Results of the iterative iceberg detector.

Data set	Number of missed hits	Number of false alarms	False alarms per km²
1	2	41	0.023
2	2	0	0
3	0	4	0.004
4	0	3	0.001
5	0	0	0
6	5	0	0
7	2	1	0.002
8	0	0	0
9	1	0	0
10	0	1	0.001
11	1	0	0
12	0	0	0
13	1	0	0
14	2	0	0
Sum	16	50	Mean = 0.003

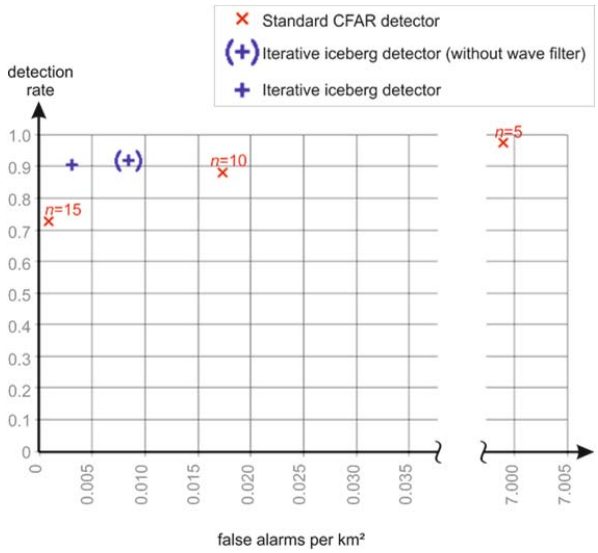

Figure 10. Comparison of different detectors.

Scientific use

The iterative iceberg detector presented in this paper is designed to support ship routing in ice frequented areas. Beyond that, it may also improve associated works in polar research, e.g. observations on iceberg frequency, iceberg collapse, or ice concentration. As a case study, we analyze the TerraSAR-X image of data set 14 (**Table 2**). While the previous experiment focused on an ROI in which *in situ* data are available, we now analyze the complete scene (**Figure 11**).

Utilizing the iterative iceberg detector, 6,873 icebergs were detected in the scene. From the binary output image, we calculated the iceberg coverage map depicted in **Figure 12**. The resolution of the map is ten times smaller than the resolution of the input image, i.e. for map generation, the binary output image is partitioned into (non-overlapping)

10x10 pixel patches in checkerboard pattern. For each such patch, we compute the percentage of detected iceberg pixels. These percentage values, in original geometric order, then form the iceberg coverage map.

The iceberg coverage map in **Figure 12** reveals an expanded area of high iceberg density along the coast. This coincides well with field observations.

Conclusion

In this paper, we proposed an automatic algorithm for iceberg detection from high resolution X-band SAR data. It is based on the iterative censoring CFAR detector, which has proven its usefulness already for target detection in dense traffic situations. However, we are the first to apply to the iceberg detection problem. In order to better discriminate icebergs from false alarms that frequently arise from rough seas and strong winds, we included a novel filter, taking into account the outer shape of detected objects. Detections that are part of a recurring pattern (such as waves) are filtered out. The "wave filter" reduces the false alarm rate significantly.

Furthermore, two minor modifications on the CFAR detector make a contribution to the results: First, gradient information is used to roughly distinguish between iceberg pixels and open water pixels in the very first iteration step, which speeds up the iterative approach. Second, a front side driven region growing is added in order to merge pixels that belong to one iceberg into an iceberg region and - in so doing - map icebergs more accurately.

We tested the algorithm with a series of HH polarized TerraSAR-X Stripmap images covering different sea state and wind conditions (wind speed up to 16.7 m/s) and different incidence angles (from 24.0° to 39.7°). Overall, we recorded a detection rate of about 90 %. The false alarm rate is kept down at 0.003 false alarms per km². The wave filter on its own reduced the false alarm rate by factor three, while the detection rate is only marginally affected.

In comparison, the standard (i.e. non iterative) n-sigma CFAR detector achieves a detection rate ≥ 90 % at $n < 10$, but this is accompanied by a false alarm rate at least five times higher than the false alarm rate of the proposed iterative algorithm. A lower false alarm rate (approx. 0.003 false alarms per km²) is reached with the standard CFAR detector at $n = 15$, but at the same time the detection rate is reduced. To sum up, the proposed iterative algorithm optimizes both, the detection rate and the false alarm rate.

Results are output within 12 minutes of computing time. This provides us with the basis for supporting operational services on ship routing in ice frequented waters.

Future works

Although the wave filter shows promise for reducing the false alarm rate, upcoming research will focus on further reduction of false alarms. Since by now the filter is based on the nonrectangular CFAR concept, it expresses the probability that a detection is "not representing water". We want to add a quality measure that expresses the probability of "representing ice". Both quality measures can be fused in terms of

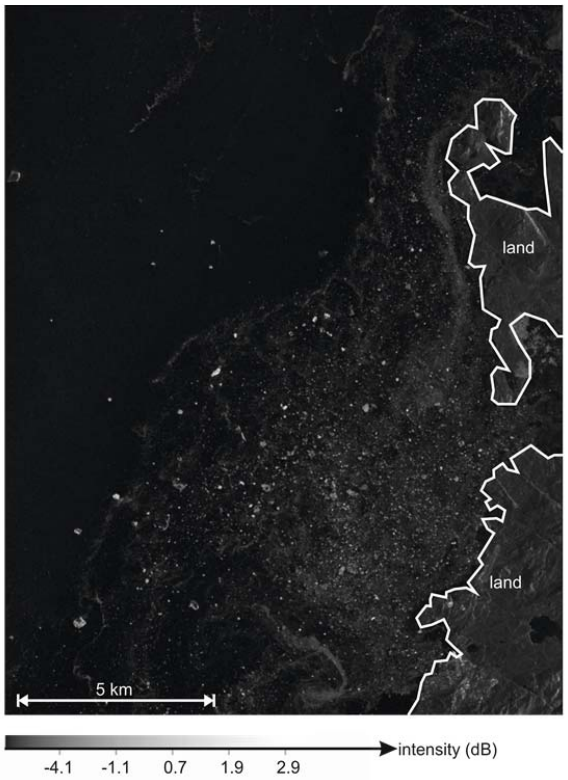

Figure 11. Section of a TerraSAR-X Stripmap image taken over Disko Bay off the Jakobshavn Glacier, Greenland, 2014/10/09.

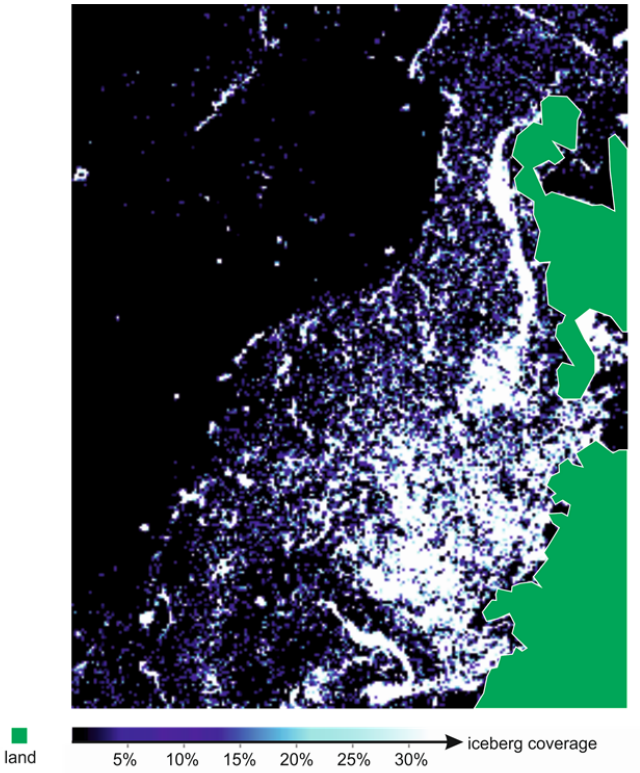

Figure 12. Iceberg coverage map generated from the TerraSAR-X image shown in **Figure 11**.

Dempster's rule of combination as applied by Ike (2011) and Frost et al. (2012). Further improvements in the recognition of false alarms might be expected.

The iterative iceberg detector detects ships as icebergs. In practice, ships have to be sorted out from the detection results manually. In ongoing work, we utilize a neural network for automated differentiation of icebergs and ships (Bentes et al., 2016).

Acknowledgment

We acknowledge Airbus D&S for providing the TerraSAR-X data sets 8, 9, and 12.

We thank C-CORE for supporting the record of ground truth data in the footprint of data set 13.

References

Bentes, C., Velotto, D., and Lehner, S. 2014. Analysis of ship size detectability over different TerraSAR-X modes. In *Geoscience and Remote Sensing Symposium (IGARSS)*, 13-18 July 2014, Quebec City, Canada. IEEE International, pp. 5137 - 5140.

Bentes, C., Frost, A., Velotto, D., and Tings, B. 2016. Ship-Iceberg Discrimination with Convolutional Neural Networks in High Resolution SAR Images. In *EUSAR 2016*

Brekke, C. 2008. *Automatic ship detection based on satellite SAR*. FFI rapport.

Brusch, S., Lehner, S., Fritz, T., Soccorsi, M., Soloviev, A., and Van Schie, B. 2011. Ship surveillance with TerraSAR-X. *IEEE Transactions on Geoscience and Remote Sensing*, 49(3), pp. 1092-1103.

Buus-Hinkler, J., Qvistgaard, K., and Harnvig Krane, K.A. 2014. Iceberg number density – Reaching a full picture of the Greenland waters. In *Geoscience and Remote Sensing Symposium (IGARSS)*, 13-18 July 2014, Quebec City, Canada. IEEE International. pp. 270 – 273.

Diemand, D. 2001. Icebergs. *Academic Press*, pp. 1255-1264.

Eineder, M., Fritz, T., Mittermayer, J., Roth, A., Boerner, E., and Breit, H. 2008. *TerraSAR-X Ground Segment, Basic Product Specification Document*. Cluster Applied Remote Sensing (CAF), Oberpfaffenhofen, Germany. Report No. TX-GS-DD-3302.

El-Darymli, K., McGuire, P., Power, D., and Moloney, C. 2013. Target detection in synthetic aperture radar imagery: a state-of-the-art survey. *Journal of Applied Remote Sensing*, 7(1).

Frost, A., Renners, E., Hötter, M., and Ostermann, J. 2012. Probabilistic evaluation of three-dimensional reconstructions from X-ray images spanning a limited angle. *Sensors*, 13(1), pp. 137-151.

Gao, G., Liu, L., Zhao, L., Shi, G., and Kuang, G. 2009. An adaptive and fast CFAR algorithm based on automatic censoring for target detection in high-resolution SAR images. *IEEE Transactions on Geoscience and Remote Sensing*, 47(6), pp. 1685-1697.

Gill, R.S. 2001. Operational detection of sea ice edges and icebergs using SAR. *Canadian journal of remote sensing*, 27(5), pp. 411-432.

Howell, C., Youden, J., Lane, K., Power, D., Randell, C., and Flett, D. 2004. Iceberg and ship discrimination with ENVISAT multipolarization ASAR. In *Geoscience and Remote Sensing Symposium,* 20-24 September 2004, IEEE International.

Ike, T. 2011. *Evidenzbasierte Analyse interner Konflikte bei der Fusion komplementärer Fahrzeugumfeldbeschreibungen*. VDI Verlag, Düsseldorf, Germany. Fortschrittsberichte Reihe 12, No. 736.

Lehner, S., Krumpen, T., Frost, A., Ressel, R., Busche, T.E., and Schwarz, E. 2014. First tests on near real time ice type classification in Antarctica. In *Geoscience and Remote Sensing Symposium (IGARSS)*, 13-18 July 2014, Quebec City, Canada. IEEE International, pp. 4876-4879.

Power, D., Youden, J., Lane, K., Randell, C., and Flett, D. 2001. Iceberg detection capabilities of RADARSAT synthetic aperture radar. *Canadian Journal of Remote Sensing*, 27(5), pp. 476-486.

Principe, J.C., Radisavljevic, A., Kim, M., Fisher III, J., Hiett, M., and Novak, L.M. 1995. Target prescreening based on 2D gamma kernels. In *SPIE Proceedings,* Vol. 2487, pp. 251-258.

Ren, Y., Lehner, S., Brusch, S., Li, X., and He, M. 2012. An algorithm for the retrieval of sea surface wind fields using X-band TerraSAR-X data. *International journal of remote sensing*, 33(23), pp. 7310-7336.

Ressel, R., Frost, A., and Lehner, S. 2015. Navigation Assistance for Ice-Infested Waters through Automatic Iceberg Detection and Ice Classification Based on TerraSAR-X Imagery. *International Archives of the Photogrammetry*, Remote Sensing and Spatial Information Sciences.

Scharf, L.L. 1991. *Statistical signal processing*. Reading, MA: Addison-Wesley.

Shao, W., Li, X. M., Lehner, S., and Guan, C. 2014. Development of polarization ratio model for sea surface wind field retrieval from TerraSAR-X HH polarization data. *International Journal of Remote Sensing*, 35(11-12), pp. 4046-4063.

Truckenbrodt, J. 2012. *Bestimmung und Validierung von U10 Windfeldern aus TerraSAR-X Daten und deren Nutzung für operationelle Schiffsdetektion*. Thesis. University of Jena, Germany.

Vachon, P.W., Campbell, J.W.M., Bjerkelund, C.A., Dobson, F.W., and Rey, M.T. 1997. Ship detection by the RADARSAT SAR: Validation of detection model predictions. *Canadian Journal of Remote Sensing*, 23(1), pp. 48-59.